Nuclear Instruments and Methods in Physics Research A 395 (1997) 328–343

ELSEVIER

NUCLEAR INSTRUMENTS & METHODS IN PHYSICS RESEARCH Section A

3D – A proposed new architecture for solid-state radiation detectors[1]

S.I. Parker[a,*], C.J. Kenney[a], J. Segal[b]

[a] *University of Hawaii, Honolulu, USA*
[b] *Integrated Circuits Laboratory, Stanford University, Stanford, USA*

Abstract

A proposed new architecture for solid-state radiation detectors using a three-dimensional array of electrodes that penetrate into the detector bulk is described. Proposed fabrication steps are listed. Collection distances and calculated collection times are about one order of magnitude less than those of planar technology strip and pixel detectors with electrodes confined to the detector surface, and depletion voltages are about two orders of magnitude lower. Maximum substrate thickness, often an important consideration for X-ray and gamma-ray detection, is constrained by the electrode length rather than by material purity or depletion-depth limitations due to voltage breakdown. Maximum drift distance should no longer be a significant limitation for GaAs detectors fabricated with this technology, and collection times could be much less than one nanosecond. The ability of silicon detectors to operate in the presence of the severe bulk radiation damage expected at high-intensity colliders should also be greatly increased.

1. Introduction

Since the development of silicon detectors with surface barrier electrodes in the 1960s and ion-implanted ones in the 1980s [1], planar structures on the material surfaces have been used. Voltages that are typically many tens of volts are needed to deplete the detector bulk which is normally hundreds of microns thick. Typical drift paths for ionization charges are at least comparable to that thickness. The structure proposed here uses electrodes with typical pitches of a few tens of microns and which penetrate from one surface through most or all of the bulk (see Fig. 1). The resulting short charge collection distances provide fast collection and low-depletion voltages. Short collection times will be useful for a proposed quantum mammography system [2] which records individual X-ray hit locations, and the combination will be particularly useful at high-luminosity colliders where detectors face severe problems both from high event rates and from increased depletion voltages due to bulk radiation damage. Use of this technology should eliminate bulk type-reversals, any need for high-depletion voltages, and the need to refrigerate the detector continuously, even during maintenance.

The key facts that make this technology possible are:

(1) Deep, reactive-ion etching now permits holes to be made with depth-to-width ratios of over 15:1 and with silicon-to-oxide-mask etch rate selectivity of greater than 300:1 or silicon-to-photoresist selectivity of greater than 50:1 [3]. Absolute etch rates (about 5 μm/min) are also high.

(2) The holes can then be filled with silicon made by the surface reaction of silane, which will bounce off the silicon surfaces thousands of times before reacting, thus depositing silicon as readily near the bottom as well as the top [4].

(3) Similar behavior by dopant gases such as diborane and phosphine, when added to the silane, allows the fabrication of n +- and p +- electrodes. All of the three gases will form conformal coatings without clogging the top of the hole before the bottom can be covered [4, 5].

(4) The silicon layers deposited simultaneously on the wafer surfaces will have a thickness somewhat greater than the hole radius, and can be readily removed by etching.

The fabrication steps following electrode formation can be varied to produce monolithic pixel detectors [6],

* Correspondence address: MS 50B-6208, Lawrence Berkeley Laboratory, Berkeley, CA 94720, USA. Tel.: +1 510 486 5859; e-mail: sher@slac.stanford.edu.

[1] This work was supported by the U.S. Department of Energy under grant DE-FG03-94ER40833.

PII S0168-9002(97)00694-3

bump-bonded pixel detectors [7], and strip detectors with or without on-chip driving electronics associated with the bulk electrodes. Proposed devices of each type will be described, with the most detail for the simplest ones, which we plan to fabricate first: diodes for DC and capacitance tests and for bump-bonded pixel detectors. Although we are concentrating here on a silicon device, it is possible that GaAs ones could benefit even more, as large thicknesses could provide good X-ray and gamma-ray detection efficiencies but for their drift-length limitations. Here it could be possible to provide electrode spacings that are less than those drift length limitations. The short maximum drift distances combined with the high electron mobility of GaAs will also produce an extremely fast detector.

2. A basic detector for initial tests and for bump-bonded pixels

Many different electrode arrangements could be used, depending on the requirements of the test devices and of any experiment using pixel detectors. Fig. 1 shows a view of one possible basic PIN diode cell. Some of the architectural principles used in previously-fabricated, monolithic pixel detectors [6] are also used here:

(1) If it is necessary to minimize the maximum electric fields, electrodes forming the diode junctions will have more total surface area than those forming ohmic ones.

(2) N +- electrodes have phosphorus doping and serve as getters. Their area is kept as large as possible consistent with other design requirements.

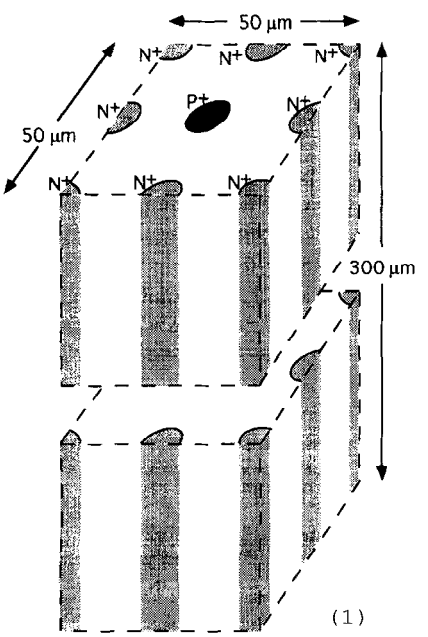

Fig. 1. Three-dimensional view of a typical cell.

(3) Use of p^{--}-substrate prevents type change from bulk radiation damage which, while not necessarily lethal in all designs, does mess up principle (1). There is also data, though not at high fluence, indicating p^{--} silicon is less subject to bulk damage than n^{--} [8].

These three imply the p-electrode should transmit the signal from the entire pixel while the multiple n-electrodes form the diode junctions. Signals could be taken from them also, further subdividing the pixel, and also providing faster signal collection speed, but monolithic technology is likely to be needed for the smallest read out pitches. With fast electronics, improved position and time information could also be provided by comparing the various p and n signal times and pulse heights.

In addition,

(4) To reduce the number of bumps required, and to provide redundancy for those that are used, multiple n electrodes are tied together with metal or diffusion conductors, as are the electrodes in many test structures. If the desired amount of electronics in the pixel causes the pixel area to exceed the area of the underlying bulk cell, conductors can also be used to join p-electrodes from several cells to the pixel electronics, but with the price of increased capacity $\sum C_i$, a reduced signal, $q/\sum C_i$, and a reduced signal-to-noise ratio. In this case, one simple front-end circuit per cell with an input signal q/C_i, may be a better choice. The random noise of the sum then increases, and the signal-to-noise ratio decreases, at most only as the square root of the number of cells. (For example, if one source-follower from each cell is used to drive a common pixel bus, one with a signal will tend to cut off those without, and only the noise on that channel will be present.)

When on-wafer metal lines are used, the electrode tops will be in contact with, and surrounded by an implanted ring of like-type silicon to make the contacts, as the silicon surface directly above the electrodes may not be fully planar.

(5) The silicon surfaces can be inverted by charges in the surface field oxide layers, which could make a continuous n-conductor from the n-electrodes to the immediate vicinity of the p-electrodes. This small gap, which can result in increased electrode capacity and fields, however, should be significantly enlarged by the applied depletion voltage. Increased oxide charge due to radiation damage might again reduce the gap. To prevent this, p^+-guard rings around the p electrode or a blanket p-implant may be used. Implanted rings will also be used in test devices to monitor surface leakage currents.

3. Fabrication steps for test structures and bump-bonded diodes

One possible sequence of fabrication steps is given below. Routine wafer cleaning and process checking

steps are not listed. In addition, most major steps have many sub-steps which are also not given. For instance, masking steps involve spinning on of photoresist, a low-temperature bake, exposure in a mask aligner, photoresist development, a high-temperature bake, the masked process (such as ion implantation or etching), and photoresist stripping. And even a simple step such as the spinning on of the photoresist will have sub-steps.

(1) *Mask* 1: alignment-mark mask and etch.
(2) *Mask* 2: n-electrode mask and wafer etch-through.
(3) n + -silicon deposition and hole fill (for example, using a silane/phosphine mixture).
(4) Etch back deposited silicon on both wafer surfaces.
(5) *Mask* 3: p-electrode mask and wafer etch-through.
(6) p + silicon deposition and hole fill (for example, using a silane/diborane mixture).
(7) Etch back deposited silicon on both wafer surfaces.
(8) Thermal oxidation (0.6 μm oxide thickness).
(9) Etch oxide, backside.
(10) Backside blanket p^+ implant (to prevent oxide charges from inverting the adjacent silicon; this step might not be needed or might be changed to a masked one with p^+-rings to increase the n^+/p^+ separation).
(11) Thermal oxidation (0.6 μm oxide thickness). (If step 10 is not needed, steps 9 and 11 will also be omitted.)
(12) *Mask* 4: front side n^+-mask and implant (to provide a planar ohmic contact to the n^+-electrodes – the silicon fill at the electrode surfaces will not necessarily be flat).
(13) *Mask* 5: front side p^+-mask and implant (to provide planar ohmic contact to the p^+ electrodes and guard rings around them if the rings are used to monitor currents).
(14) Anneal implants.
(15) Low-temperature oxide (LTO) deposition.
(16) *Mask* 6: contact mask and etch.
(17) Aluminum deposition.
(18) *Mask* 7: metal mask and etch.

4. Epi versus poly

Two major questions must be answered by experiment: the size of the smallest holes that can be etched through, and whether single-crystal (epi) or poly-crystalline silicon (poly) is used to fill the holes. Holes 15 μm in diameter and 200 μm deep have been made in which the top-to-bottom taper is less than 0.1 μm, and it is believed that 10 μm holes can be readily etched [9]. Epi is generally more difficult to make than poly, and can only be deposited on single-crystal silicon, which however, should form the hole surfaces, if they are properly cleaned prior to deposition. It is not clear if the nature of the etched surfaces will present extra difficulties to epi deposition.

Use of epi will provide one major advantage, particularly if it can be combined with a gradually increasing dopant level during deposition. Following the anneal, there should be a radial dopant gradient that will provide a radial built-in electric field which will transport ionization charges in the same direction as the applied field, providing rapid collection of charge from the entire volume of the detector, including the electrodes.

Following the deposition, the silicon is heated so the dopant atoms move to lattice sites and become electrically active. They also diffuse out from the n^+ electrodes into the p^{--} bulk and form p–n junctions in high-quality silicon. However, in poly, diffusion of dopant atoms, following grain boundaries, is far faster than in single crystal silicon. Because of this, a nearly uniform doping density is established in the poly, reducing the size of the built-in field in the electrodes. Diffusion of ionization charge from the track to the start of the applied field several microns away, possibly with a small boost from Coulomb repulsion from the rest of the track, becomes the only method of collection. This is discussed in more detail in Section 9. Recombination within the electrodes should not be a problem. Measurements on 20 Ω cm epi in a CCD vertex detector show diffusion lengths of about 200 μm [10].

5. Calculated performance

Voltage distributions have been calculated both by MEDICI [11] and by the sequential-over-relaxation method [12]. (We have coded the latter so its speed and efficiency permit its use in three-dimensional calculations as well as the two-dimensional ones needed for this section.) For the latter, symmetric boundary conditions, $V(i+1,j,k) = V(i-1,j,k)$, are used for the (cubic) cells on either side of a boundary at the plane i = constant, where the V's are the voltages at the center of the cells. At silicon-insulator boundaries, the next voltage for any cube is found from the average of the four adjoining ones on the boundary and the adjoining one further into the silicon (plus the usual term from fixed charges). This is a reflection of the fact that, in equilibrium, there is no net charge transport into the cube, and so the sum of the current across the five faces and thus the five voltage differences sum to zero. (In this approximation, surface currents are neglected.) The effects of induced charges are calculated using Ramo's theorem [13].

At present, of the two, only MEDICI can calculate fields and current flow in the presence of surfaces and undepleted silicon. When both methods could be used for the same problem, results agreed within errors. Coulomb forces within the ionization cloud are included but are generally unimportant, causing only about a 10% decrease in collection times, even when a track was at a zero-drift field location such as the null point between

two n^+-electrodes. (In the sequential-over-relaxation method, the Coulomb forces were approximated by subdividing the 24000 electron–hole pairs from a typical minimum-ionization track into packets of 40 charges each, which diffused and drifted as a group. Results did not change significantly when the packet size was changed.)

Depletion voltages for the sample diode shown in Fig. 1 are 1.6, 1.8, 3.8, and 8.8 V for dopant concentrations of 10^{12}, 3×10^{12}, 10^{13}, and 3×10^{13}/cc, including

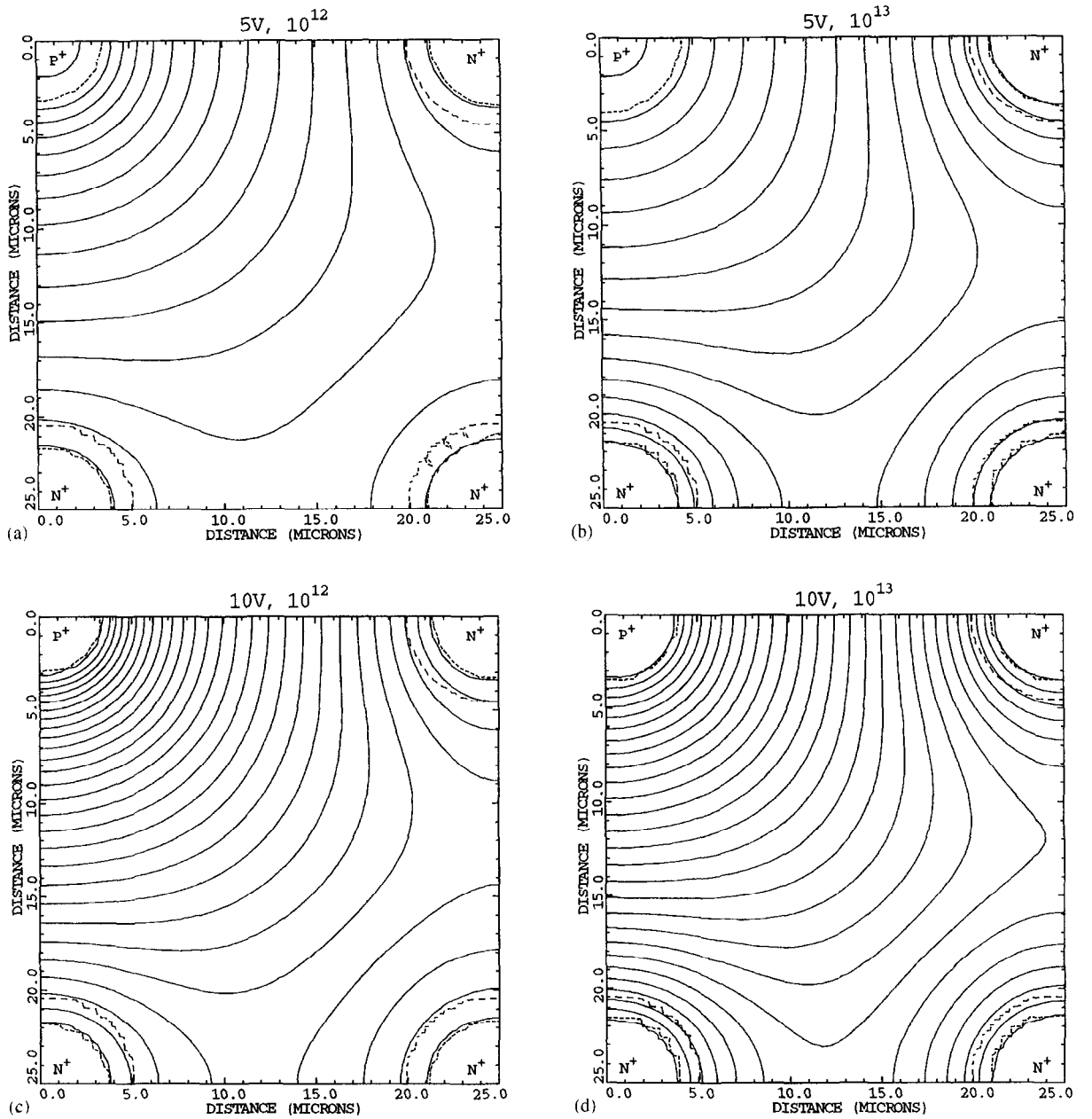

Fig. 2. (a) Equipotentials for one quarter of the unit cell of Fig. 1 with 10^{12} dopant atoms/cc when 5 V is applied between the two electrodes. The boundaries of the depleted region are indicated by short dashes. Lines with longer dashes, mark n–p junctions; (b) equipotentials for 10^{13}/cc, 5 V; (c) for 10^{12}/cc, 10 V; (d) for 10^{13}/cc, 10 V. Effects of surface charges are not included. The lack of cylindrical symmetry in the fields and depletion depths into the electrodes, especially of the n^+ ones adjacent to the p^+-electrode, can be seen as can the decrease in low-field volume for the heavier (10^{13}/cc) substrate doping.

a contribution from the built-in voltage at the electrodes that ranges from about 0.7 to 0.8 V. The values are not proportional to the concentrations because in the course of fully depleting the lightly doped silicon, part of the heavily doped region around the electrodes is also depleted. Our first and second generation pixel detectors have a doping concentration of 1.2×10^{12}/cc. Bulk damage in 10 yr for pixel detectors at the LHC would not be expected to increase this doping much beyond 10^{13}/cc.

Fig. 2(a) shows equipotentials for one quarter of the unit cell of the same device with 10^{12} dopant atoms/cc when 5 V is applied between the two metal electrodes. The cylindrical electrode doping profile assumed here and throughout this paper is $10^{18} \exp(-(r/r_0)^2)$, where r_0 is chosen to bring the concentration to 10^{12}/cc at $r = 5$ μm. This profile will produce n^+-electrodes with a resistance of about 3 Ω/μm and p^+ ones of about 2.5 times that value. The boundaries of the depleted region are indicated by short dashes. Lines with longer dashes, mark p–n junctions. Figs. 2(b)–(d), show similar equipotentials for 5 V–10^{13}/cc, 10 V–10^{12}/cc, and 10 V–10^{13}/cc. Fig. 3 shows drift lines corresponding to the equipotentials of Fig. 2(a).

Fig. 4(a)–(c) show the magnitude of the electric field of Fig. 2(a) along three electrode-to-electrode lines for 10^{12} dopant atoms/cc. For 5 V (the next-to-bottom line), more than enough for full depletion, the peak fields are more than an order of magnitude below avalanche fields which are over 100 000 V/cm. Fig. 5 shows peak fields actually decrease when the substrate doping increases by a factor of 10.

Fig. 6 shows lines of equal drift time corresponding to the equipotentials of Fig. 2(c), 10 V and 10^{12}/cc. The drift time from the center of the cell is less than 1 ns, and the times from the other electrodes ranges from 1 to 4 ns. The time from the far cell borders is infinity as the collection field goes to zero there. To get realistic times for tracks in those regions, one must add diffusion, and for ionization created near or inside electrodes, the built-in fields. This is calculated by MEDICI. Fig. 7 shows charge density contours for electrons and holes created by an ionization track of 24 000 pairs parallel to the electrodes and through the middle of the cell of Fig 2(c), which should be typical of much of the area, and through the slowest, the null point on the border between two cells.

Fig. 8 shows the current pulses on the electrodes for those two starting points. The small difference in Fig. 8a (the midpoint start) between the pulses on the two n^+-electrodes adjacent to the p^+-electrode are due to small but non-zero grid size effects. Effects of induced pulses

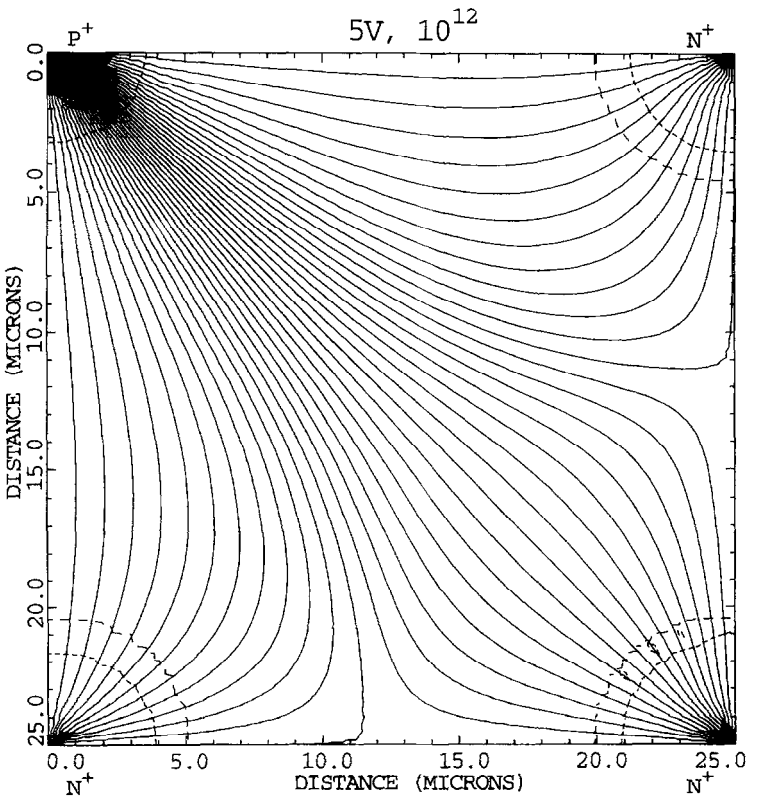

Fig. 3. Drift lines for Fig. 2(a): 10^{12} dopant atoms/cc and 5 V.

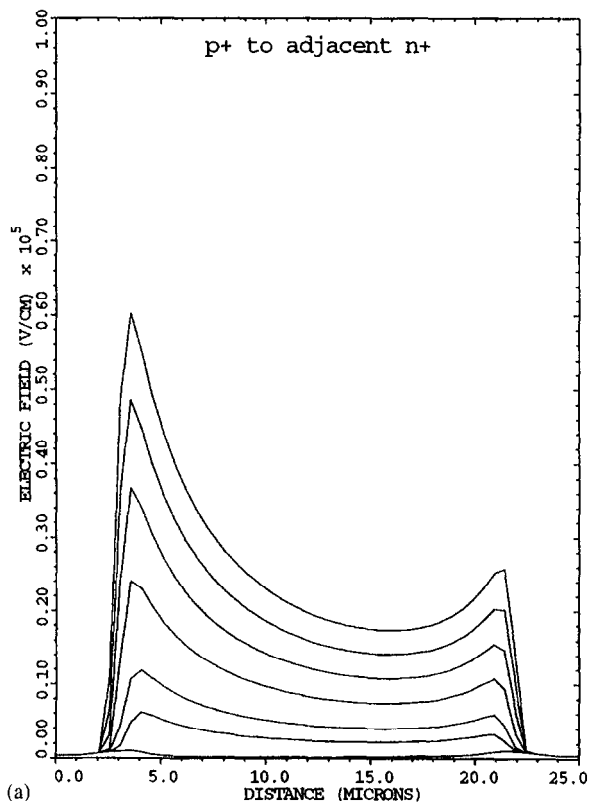

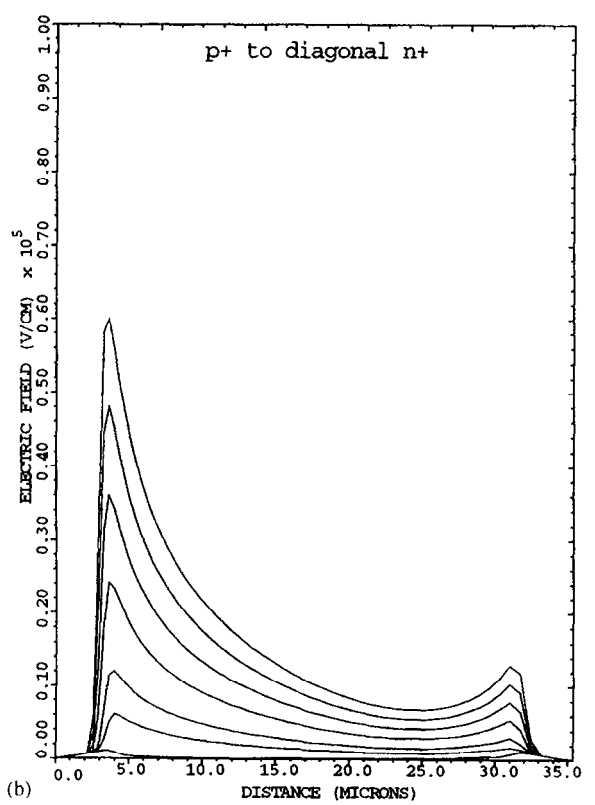

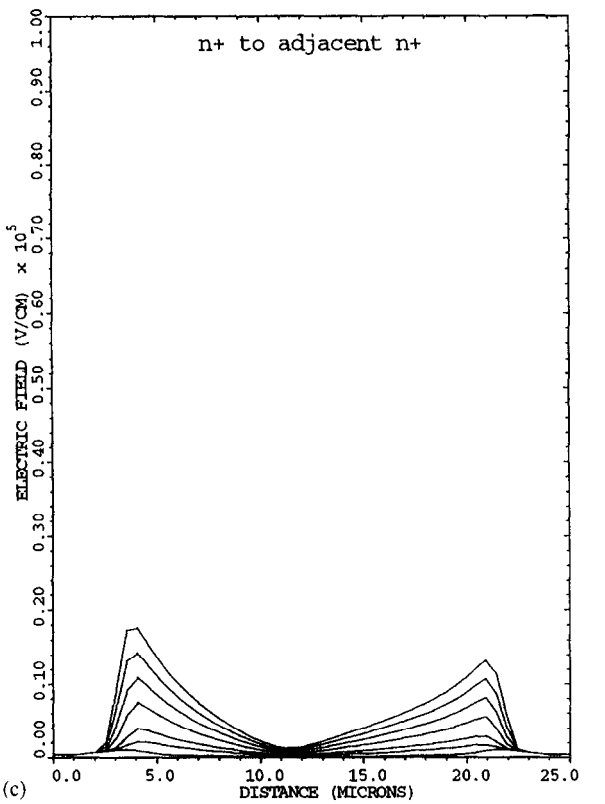

Fig. 4. Electric field magnitudes for the quarter cell of Fig. 2(a), substrate doping of 10^{12}/cc, and applied voltages of 50, 40, 30, 20, 10, 5, and 0 V (top to bottom lines) along lines from (a) the p^+ to the adjacent n^+-electrode, (b) the p^+ to the diagonally opposite n^+-electrode, and (c) the n^+ to the adjacent n^+ electrode.

from moving charges can be seen. The signal peaks at 0.5 ns and returns to the base line at 1.5 ns. Signals on strip detectors with 2D electrodes take about 25 ns to return to the baseline, neglecting amplifier delays [14]. (The return-to-baseline time can be important for pile-up considerations, especially since Landau fluctuation effects can be present until all the charge is collected.) The pulse on the p^+-electrode for the null point track (Fig. 8b) peaks at 2.4 ns, and returns to the baseline at about 6 ns. These times, while significantly shorter than typical times for detectors with 2D planar electrodes, are, at the same time, for 3D devices with far lower maximum fields.

6. Choice of electrode diameter and wafer thickness

Factors entering into the choice of hole diameter, in addition to fabrication capabilities, are the electrode capacitance, which is made smaller – improved – for small diameters, and the resistance and maximum electric fields which are increased, and so made worse.

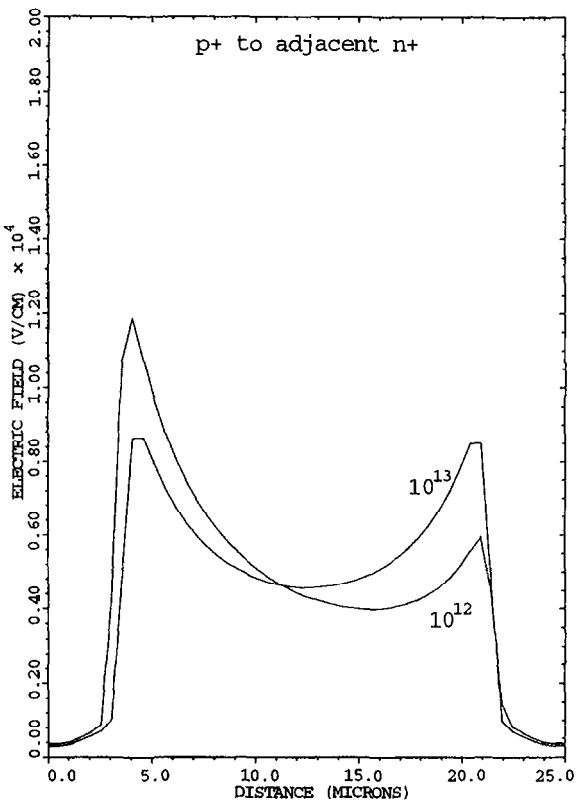

Fig. 5. Comparison of electric field magnitudes for the quarter cell of Fig. 2, 10 V applied voltage, along the line from the p^+- to the adjacent n^+-electrode for substrate dopings of 10^{12}/cc and 10^{13}/cc. With higher substrate dopant levels, as can occur with radiation damage, the peak fields, located where the depletion volume meets the electrodes, actually decrease due to the increase in voltage dropped across the lightly doped (compared to the electrodes) substrate. The small, but non-zero values of the electric fields at the ends of the plot (corresponding to the electrode centers) are due to approximations in the finite-element calculations.

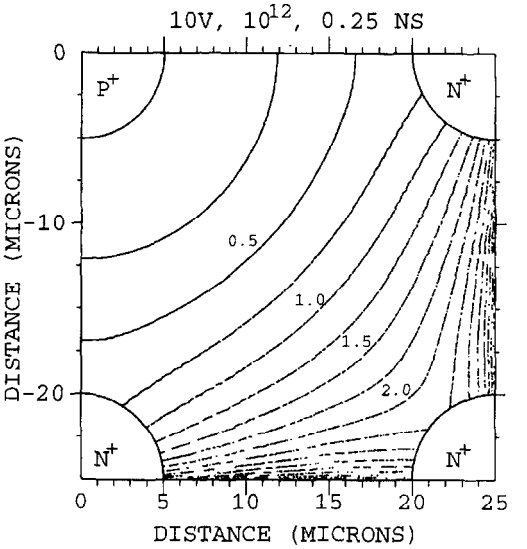

Fig. 6. Lines of equal drift time for potential distributions of Fig. 2(c) (10^{12}/cc and 10 V). Zero time is measured from the p^+-electrode (top left corner) at $r = 5$ μm and charges are traced backwards. Lines in the immediate vicinity of the zero-field points at the bottom center and right center are not reliable: diffusion plays a major role there. In addition, few of the tracks being traced backwards go there.

The capacitance, C, of a 300 μm long electrode is about 0.1 pF. The RC products, related to the minimum times pulses take to leave the electrodes, are about 90 and 225 ps for the n^+- and p^+-electrodes. For some (but not all) structures, the value of R may also play a role in the noise performance, but that depends sensitively on the circuit to which the electrode is connected and is beyond the scope of this paper. Other possible fabrication sequences, for instance ones using selective deposition of tungsten in the central core of the holes to reduce the value of R, will not be needed for pixel detectors which are the first planned application of this technology, and will also not be covered here.

The initial signal developed on the electrodes, $q/C_{\text{electrode}}$, is, to first order, independent of the wafer thickness for penetrating ionizing particles as $C_{\text{electrode}}$ is approximately proportional to the thickness. While, in later stages of some electronic read out systems, thinner wafers may produce smaller signals, the degradation of the signal-to-noise ratio is not likely to be as rapid as it would be with planar, 2D electrode systems. If multiple Coulomb scattering considerations make thinner detectors desirable, it is likely, rather, that fabrication and handling difficulties will set the lower limit. Thinner wafers should actually permit smaller hole diameters to be fabricated, resulting in a decrease in $C_{\text{electrode}}$.

7. Surface effects

All of the preceding calculations are for charge motion in the detector bulk. Close to the top and bottom, the effects of surface charges and structures must be considered. Results of calculations using a simple two-dimensional model in which the n^+- and p^+-electrodes are flat slabs separated by a 15 μm region of silicon with 10^{12} acceptors/cc and covered with an oxide layer having 10^{11} positive interface charges per sq. cm., are shown in Fig. 9. A layer of induced electrons can be seen nearly reaching the p^+-electrode. When a bias is applied to the electrodes a gap appears. While this indicates it may not be necessary to use p^+-guard rings around the top of the p^+ electrode, they may be needed for radiation damaged oxides with larger surface charges.

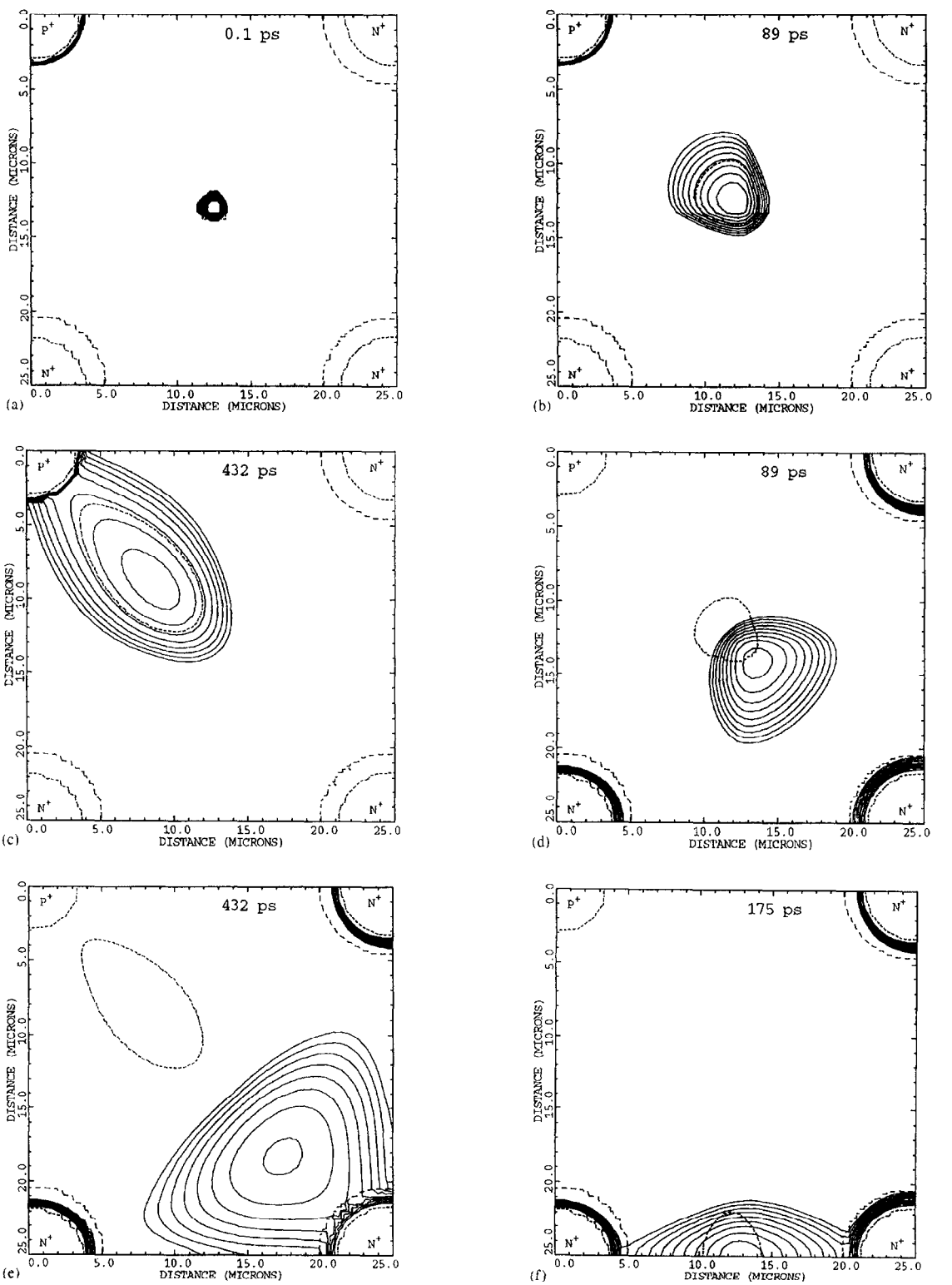

Fig. 7. Charge density contours (2 per decade) for electron – hole pairs. (a)–(c) holes starting from the cell center at 0.1, 89, and 432 ps, (d)–(e) electrons from the cell center at 89 and 432 ps, (f) electrons from the null point at 175 ps, and (g)–(l) holes from the null point at 0.1, 175 ps, 1.7, 3, 4, and 5 ns. The fields are those of Fig. 2(c), 10^{12}/cc, 10 V.

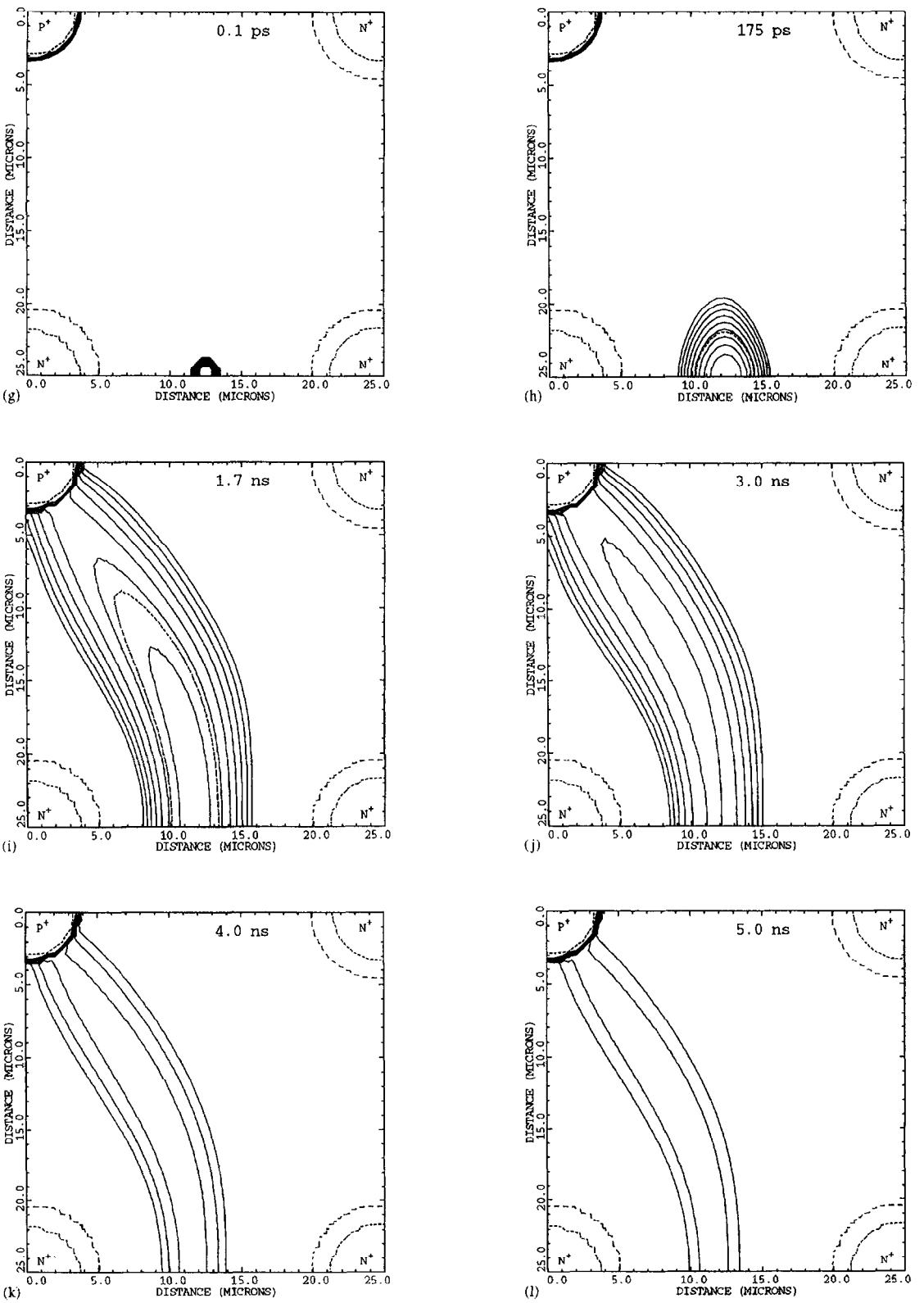

Fig. 7. Continued.

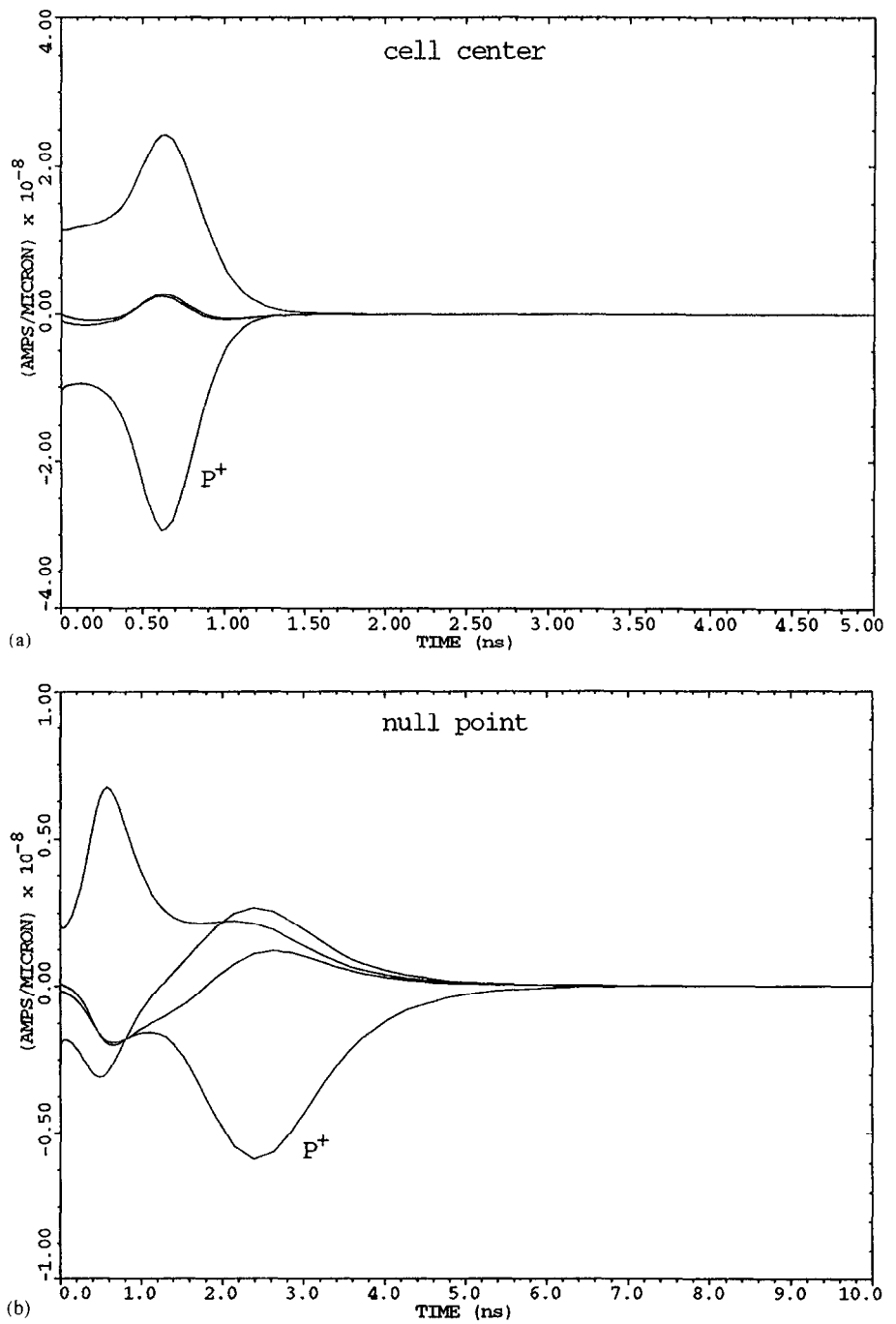

Fig. 8. Current pulses on the electrodes from a track parallel to the electrodes (a) through the cell center, and (b) through the null point between two n^+ electrodes. The fields are those of Fig. 2(c), 10^{12}/cc, 10 V. Effects of induced pulses from moving charges and diffusion are included, but not Landau fluctuations or Coulomb forces from the other charges along the track.

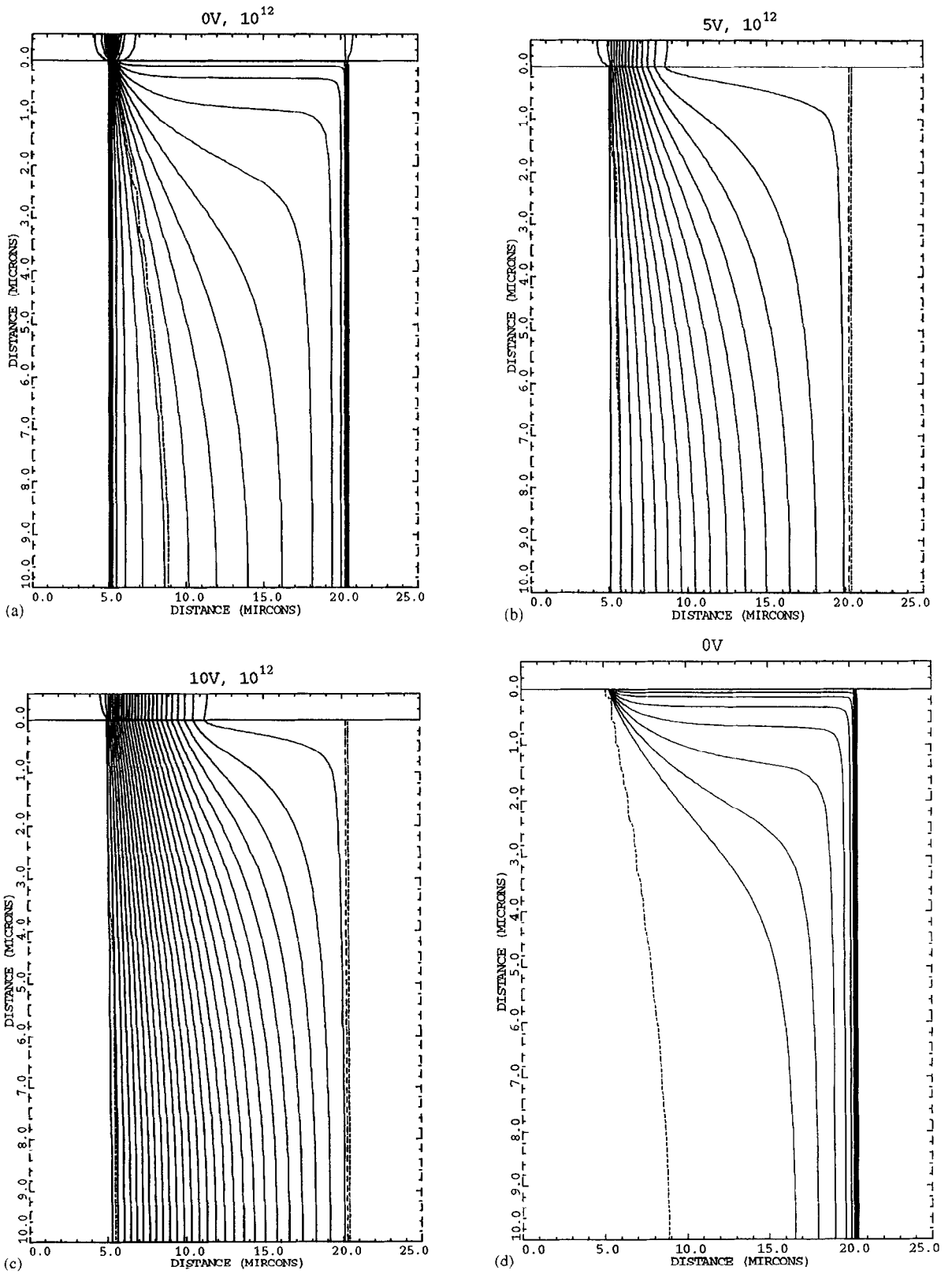
0V, 10^12
5V, 10^12
10V, 10^12
0V
DISTANCE (MICRONS)
DISTANCE (MIRCONS)
0.0
5.0
10.0
15.0
20.0
25.0
(a)
(b)
(c)
(d)

Fig. 9. a–d

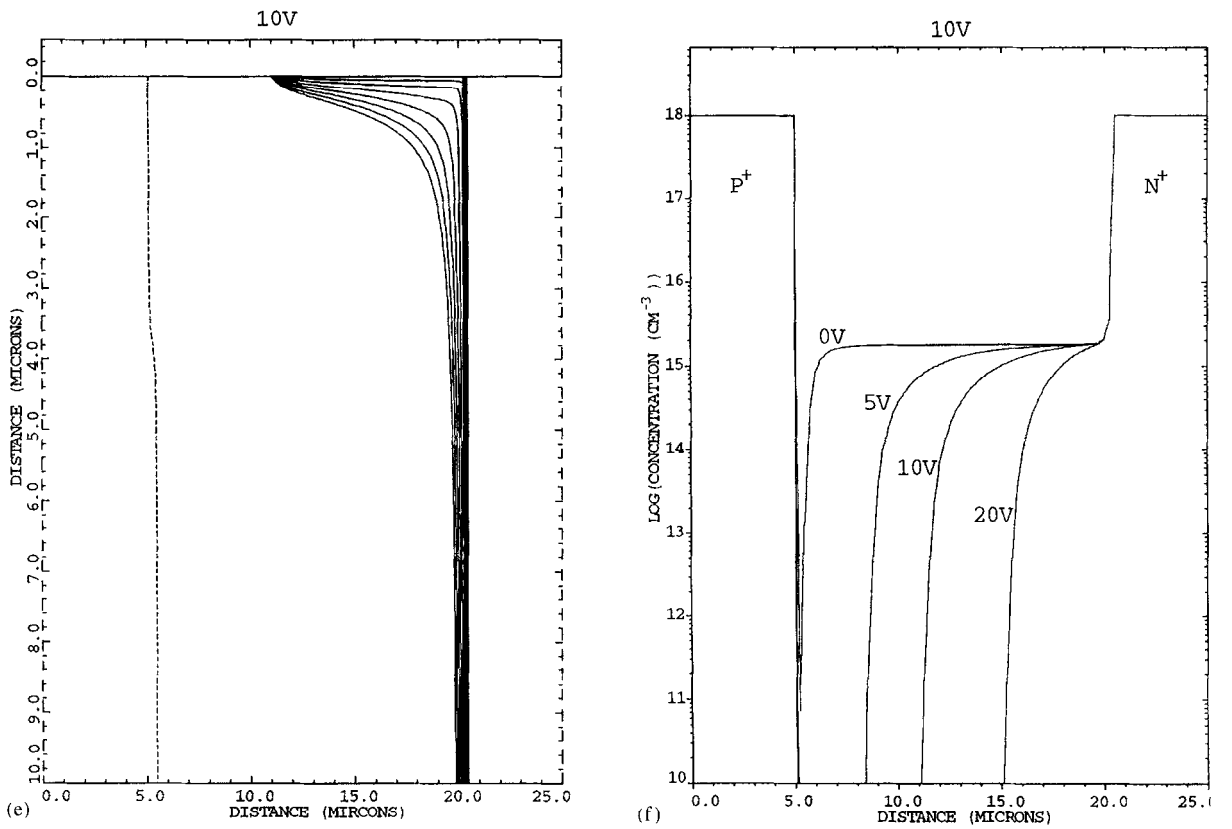

Fig. 9. Effects of an oxide interface charge of $10^{11}/cm^2$. In this two-dimensional example, the p^+- and n^+-electrodes are at 0–5 μm and 20–25 μm, doped throughout at $10^{18}/cc$, and the charges are along the top between them. The substrate doping is $10^{12}/cc$. (a) Applied voltage = 0 V. The effect of negative charge induced by the oxide charge can be seen with the closest equipotential almost parallel to the surface. The contact of the induced charge with the n^+-electrode on the right forces the equipotentials from the built-in field into a bundle next to the p^+-electrode. The capacitance between the two electrodes will be relatively high. (b) Similar equipotentials for 5 V and, (c) 10 V. An increasingly wider depletion zone at the surface can be seen. (d)–(e) Electron density contours for 0 and 10 V. (f) Net carrier concentration 0.1 μm below the surface for 0, 5, 10, and 20 V.

8. Other configurations

Fig. 10 shows several additional configurations using 3D technology. Figs. 10(a) and (b) show top views of alternating rows of n- and p-electrodes and (c) of one with hexagonal cells. Fig. 10(d) shows a side view with an implanted n-well on the top and an n^+-layer on the bottom. The n^+-layer would be made by driving phosphorus into single-crystal silicon from a poly layer, providing gettering from both phosphorus and poly [15]. Figs. 10(e)–(h) show additional side views with various combinations of wells, n^+-layers, and oxide layers with and without p^+-rings. Figs. 10(d) and (e) require backside lithography. This should not be too difficult using steps already developed to protect the wafer bottom side during lithography [6], since the structures are relatively crude and the holes provide alignment marks. Figs. 10(g) and (h) show electrodes that stop short of the bottom. This will permit a (conducting) n^+-layer to be implanted without the need for double-sided patterning. In general, cells with n^+-layers are the easiest to deplete, and those with p^+-rings the most difficult. On the other hand, the n^+-layer, forming an equipotential, normally at the same voltage as the n electrodes, will make regions with relatively slow drift velocities, as would any top wells in monolithic devices. These should not affect the main part of a pulse from an ionizing particle, but could add somewhat to the tail.

Fig. 11 shows equipotentials for one cell of Fig. 10(a), for 10^{12} net dopant atoms/cc, and 10 V applied bias. Figs. 12(a) and (b) show the electric field magnitudes for Fig. 10(a) along a line connecting an n^+ electrode with a p^+ one directly opposite, and along a parallel line through the middle of the cell. Fig. 13 shows a potential distribution for the cell of Fig. 10(c). Should poly electrodes be used, ones that penetrate only partially way might be useful, if charge collection speed or efficiency for the small number of tracks that are fully contained in the

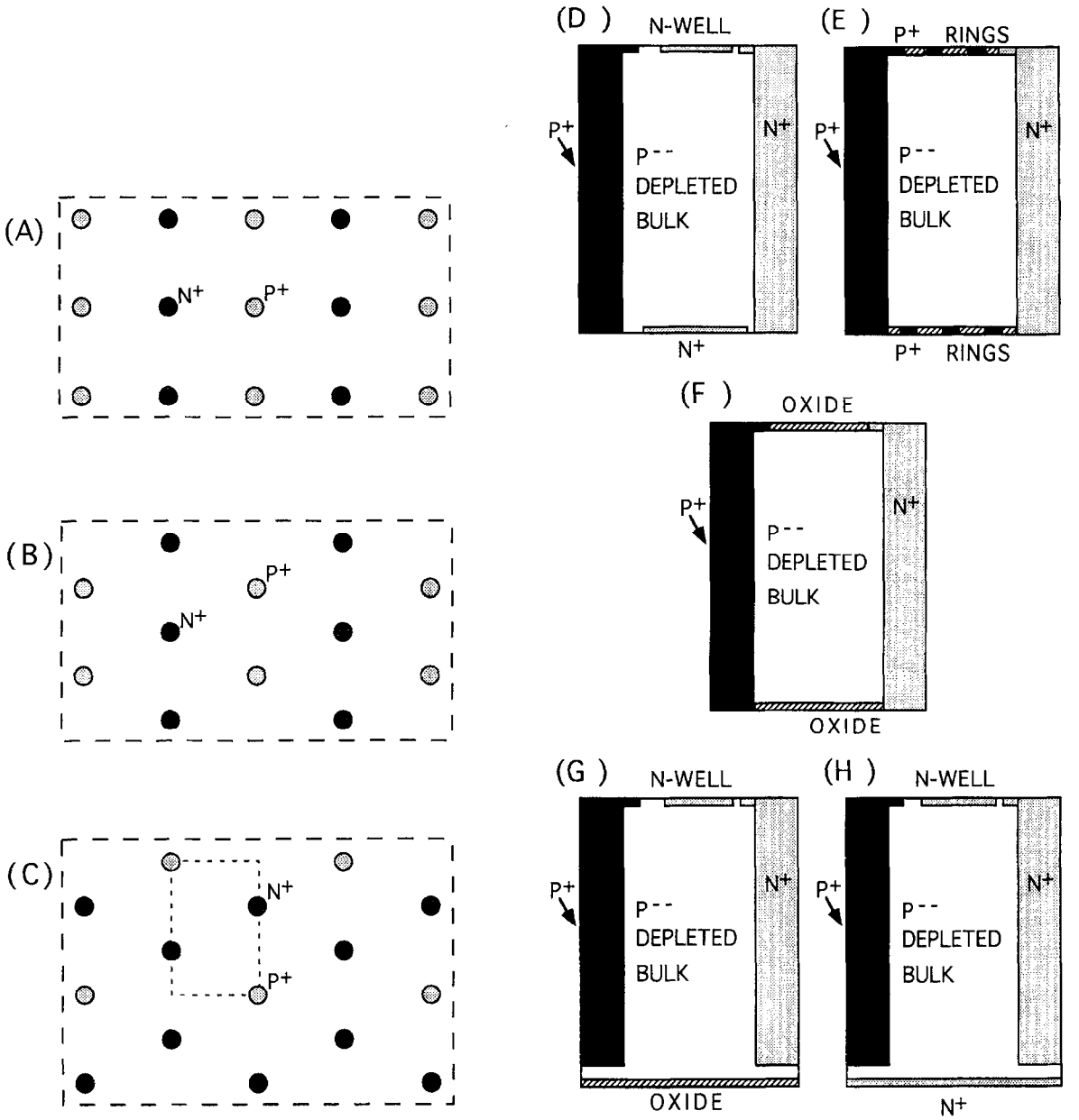

Fig. 10. Top views (a)–(c), and side views (d)–(h) of several possible structures.

electrodes prove to be lower than needed. All tracks will then make signals in the section of silicon below the electrodes. (Another way, of course, would be to glue two etched-through detectors together with an offset.)

Small wells, covering only part of the top, could be used to hold simple driving electronics for a strip read out, such as is planned for a possible mammography detector [2]. Electronics that places differential signals on twin x and twin u or y lines that drive differential receivers, would permit two-dimensional readout using single-sided technology. There would be negligible danger of interference between crossing signals, given the double subtraction at the crossing and at the receiver. The signal height would be nearly independent of the strip length, and incoherent noise would grow no faster than the square root of the length. For small-angle stereo,

it would allow read out from the ends only, since u lines reaching one edge could be crossed over the x lines and brought to the other edge from which they would continue at their stereo angle.

9. Charge collection from electrodes

Charge from tracks contained within the electrodes will leave them by diffusion and, for epi electrodes, from electric forces due to the built-in fields. Coulomb forces within the ionization charge cloud itself can either hinder or help charge collection once part of the charge has been collected. For example, in the case of floating n^+-electrodes, once some holes have diffused out to the collection field and have been removed, the net negative charge will tend to attract the remaining holes, slowing their diffusion out of the electrode. If, however, the electrons have been collected by electronics connected to the n^+-electrode, there will be a net repulsion that will speed up hole collection.

The fraction of tracks contained entirely within an electrode depends on their angular distribution as well as the electrode cross-sectional area. Table 1 shows, for an

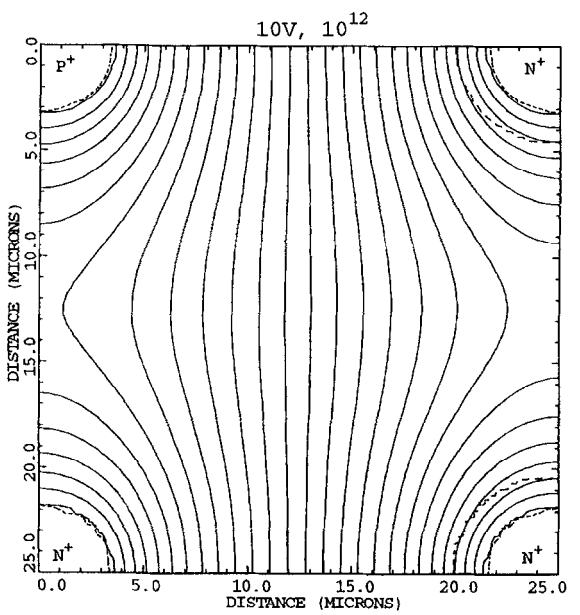

Fig. 11. Equipotentials for a cell of Fig. 10(a), 10^{12}/cc doping, 10 V.

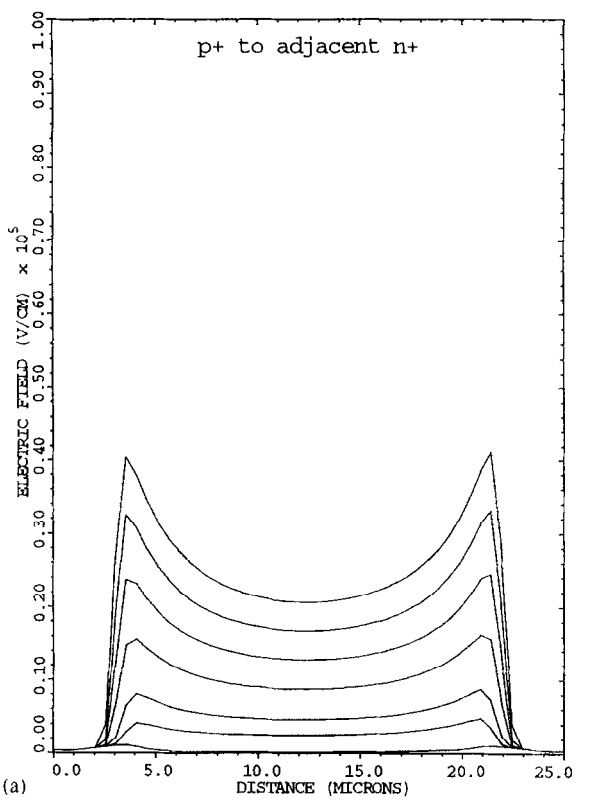

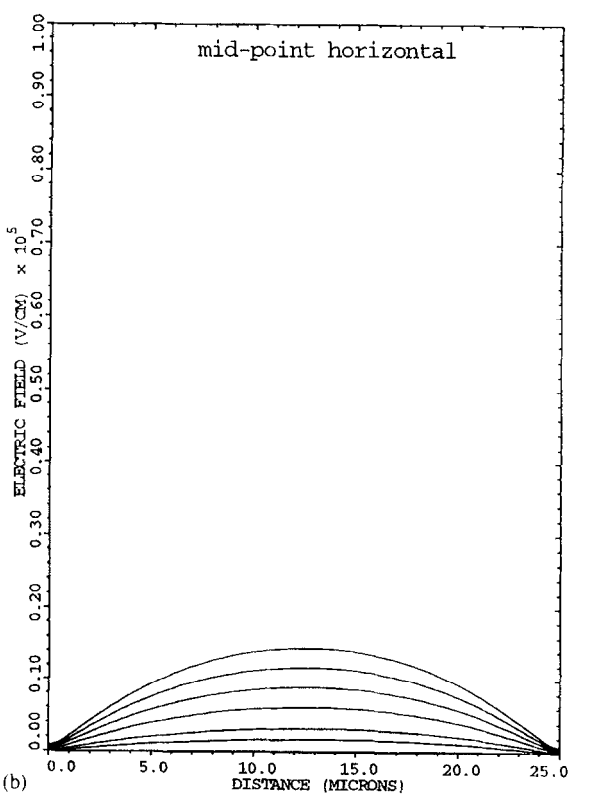

Fig. 12. Electric field magnitudes for 50, 40, 30, 20, 10, 5 V (top to bottom) of Fig. 10(a) for (a) along a line connecting a p^+ and an adjacent n^+-electrode, and (b) along a horizontal line through the middle of Fig. 11.

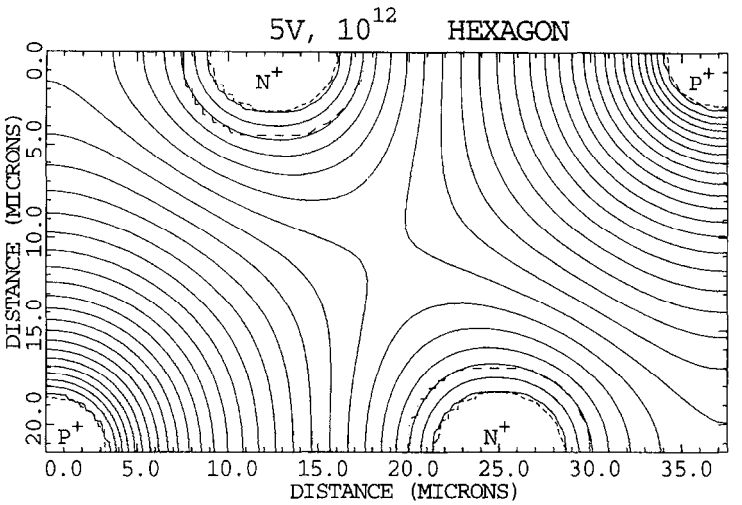

Fig. 13. Equipotentials for a cell of Fig. 10(c), 10^{12}/cc doping, 10 V.

Table 1
Pulse times for tracks at a radius r within an n^+-electrode centered in a 50 μm × 50 μm cell. The electric field within the poly is assumed to come only from other holes (e^- out – electrode connected to electronics which collects the electrons) or both holes and electrons (e^- in). Estimated errors in the times range from 5 to 10%. For poly-electrodes, the time to collect 90% of the charge is about three times that to collect 50%.

Track	r	1.0	2.0	3.0	4.0	5.0	μm
band	r_{min}	0.0	1.5	2.5	3.5	4.5	μm
	r_{max}	1.5	2.5	3.5	4.5	5.0	μm
Band area/ cell area		0.283	0.503	0.754	1.005	0.597	%
Solid angle/π		0.0025	0.0069	0.014	0.023	0.028	%
Time- epi	peak	2.9	2.7	2.3	2.2	2.1	ns
	$0.5\sum q$	3.1	2.7	2.3	2.1	2.0	ns
Time- poly, e^- out	Peak	4.5	4.1	3.5	2.4	1.9	ns
	$0.5\sum q$	6.6	5.8	4.3	2.8	1.9	ns
Time-poly, e^- in	Peak	5.1	4.7	3.5	2.5	2.0	ns
	$0.5\sum q$	8.3	6.8	4.7	3.1	1.9	ns

n^+-electrode on the diagonal between two p^+ ones of Fig. 2(c), and for several radial bands, the percentage of a 50 μm × 50 μm square cell occupied by the band. The next row shows the probability for the track to remain inside the band outer radius, for a beam distributed uniformly over π steradians centered around the normal to the detector. The probability for the entire track to stay within r_{max} is the product of the band area and solid angle factors. For a more tightly aligned beam, the product increases to that of the area fraction alone, although for very tightly aligned beams, the detector can be tilted, reducing the fully contained fraction to zero. The next two rows show the times to the pulse peak and to the 50% charge collection time for an applied voltage of 10 V and epi electrodes. The next two rows show similar times for poly electrodes without built-in fields, and with the electrons collected by the attached electronics. The final two rows are for floating poly-electrodes with the electrons left in the electrode.

Tracks will also be contained within the p^+-electrode and the two n^+-electrodes adjacent to it, roughly tripling the table area fractions. The times for these electrodes will be shorter than for the n^+ one given in the table.

10. Gallium arsenide

Similar deep holes can be etched in gallium arsenide [9] and filled using metal- organic chemical vapor deposition, for example with trimethyl gallium and arsine [16]. Such a detector would circumvent the present limitations on maximum drift distances and make an efficient X-ray

detector. With its low depletion voltages, it should be possible to keep the electric field near values that give high drift velocities, producing sub-nanosecond collection times. Combining this with the parallel processing capabilities of a pixel read out [17] would produce a detector capable of handling very high rates.

Acknowledgements

Since commercial ion-implanters have penetration ranges of only a few microns, the development of deep etching has been crucial for this technology. Many people have worked on it, particularly for micromachining applications. We would especially like to thank Kurt Petersen, Nadim Maluf, Christopher Storment, and Gregory Kovacs. Jim McVittie first let one of us know about the low sticking probability of silane, which was one of the key pieces of knowledge that led to this paper. Jim Mc Vittie, Theodore Kamins, and James S. Harris also provided valuable information on appropriate dopant gases. James Plummer has been a constant source of encouragement and advice for this and many earlier projects. Vincent Peterson and Steve Olsen have shown constant interest in our work and eliminated many near-lethal administrative barriers. Finally, we would like to thank Cinzia Davia for many interesting conversations on gallium arsenide detector developments and problems, one of which triggered the idea for this development.

References

[1] J. Kemmer, Nucl. Instr. and Meth. 226 (1984) 89.

[2] S. Parker, C. Kenney, V. Peterson, D. Ikeda, F. Backus, W. Snoeys, C.H. Aw, IEEE Trans. Nucl. Sci. 41 (1994) 2862–2873.

[3] K. Petersen, D. Gee, F. Pourahmadi, R. Craddock, J. Brown, L. Christel, Proc. Transducers 91 (1991) 397; C. Hsu, M. Schmidt, Micromachined structures fabricated using a wafer bonded sealed cavity process, Tech. Digest, IEEE S.S. Sensors Workshop, Hilton Head, SC, 1994, p. 151; E. Klaassen, K. Petersen, J. Noworolski, J. Logan, N. Maluf, J. Brown, C. Storment, W. McCulley, G. Kovacs, Transducers 95 (1995) 556; K. Murakami, Y. Wakabayashi, K. Minami, and M. Esashi, "Cryogenic dry etching for high aspect ratio microstructures", Proc. IEEE Microelectromechanical Systems Conf. Fort Lauderdale, FL, 1993 p. 65; A. Furuya, F. Shimokawa, T. Matsuura, R. Sawada, Micro-grid fabrication of fluorinated polyimide by using magnetically controlled reactive ion etching, Proc. IEEE Microelectromechanical Systems Conf. Fort Lauderdale, FL, 1993, p. 59; V. Lehmann, W. Hönlein, H. Reisinger, A. Spitzer, H. Wendt, J. Willer, Solid State Technol. 38 (Nov. 1995) 99.

[4] Jim McVittie, Center for Integrated Systems, Stanford University, Stanford CA, private communication.

[5] Theodore Kamins, Hewlett Packard Co., Palo Alto, CA, private communication.

[6] S. Parker, Nucl. Instr. and Meth. A 275 (1989) 494; W. Snoeys, J. Plummer, S. Parker, C. Kenney, IEEE Trans. Electron Devices, 41 (1994) 903; C. Kenney, S. Parker, V. Peterson, W. Snoeys, J. Plummer, C.H. Aw, Nucl. Instr. and Meth. A 342 (1994) 59.

[7] S. Gaalema, IEEE Trans. Nucl. Sci. NS-32 (1985) 417.

[8] I. Tsveybak, W. Bugg, J. Harvey, J. Walter, IEEE Trans. Nucl. Sci. 39 (1992) 1720.

[9] Christopher Storment, Stanford University, private communication.

[10] C.J.S. Damerell, Rutherford Appleton Laboratory, private communication.

[11] MEDICI, Technology Modeling Associates Inc., 3950 Fabian Way, Palo Alto, CA.

[12] K. Binns, P. Lawrenson, Analysis and computation of electric and magnetic field problems, Pergamon, 1973, p. 241.

[13] S. Ramo, Proc. IRE 27 (1939) 584.

[14] R. Sonnenblick, N. Cartiglia, B. Hubbard, J. Leslie, H.F.-W. Sadrozinski, T. Schalk, Nucl. Instr. and Meth. A 310 (1991) 189; S. Gadomski, M. Turala, E. Barberis, N. Cartiglia, J. Leslie, and H.F.-W. Sadrozinski, Nucl. Instr. and Meth. A 326 (1993) 239.

[15] S. Holland, Nucl. Instr. and Meth. A 275 (1989) 537; S. Holland, IEEE Trans. Nucl. Sci. NS-36 (1989) 283; S. Holland, H. Spieler, IEEE Trans. Nucl. Sci. NS-37 (1990) 463.

[16] James S. Harris, Stanford University, private communication.

[17] J. Millaud, D. Nygren, The column architecture – a novel architecture for event driven 2D pixel imagers, IEEE Trans. Nucl. Sci. NS-43 (1996) 1700.